

The Dosimetric Evaluation of An In-House Software Developed For Metal Artefact Reduction On Two Different Radiotherapy Treatment Planning Systems

Aysun Inal

University of Health Sciences Antalya Training and Research Hospital

Songul Barlaz Us (✉ barlaz@gmail.com)

Mersin University

Research Article

Keywords: computed tomography, metal artefact reduction, radiotherapy, MATLAB

Posted Date: April 30th, 2021

DOI: <https://doi.org/10.21203/rs.3.rs-383784/v1>

License:  This work is licensed under a Creative Commons Attribution 4.0 International License.

[Read Full License](#)

Abstract

Metal Artefact Reduction (MAR) is very important in terms of dose calculation in radiotherapy. It was aimed to develop an in-house MAR software as an alternative to commercial software programs and to examine its effectiveness by comparing it with the SMART-MAR software which was available commercially. A phantom containing metal with high atomic number was designed and computed tomography (CT) images of this phantom were taken (Without-MAR images). The obtained CT images were processed with the SMART-MAR software and the developed In-House MAR software. Processed images were compared in terms of Hounsfield unit (HU), absolute dose values in the Accuray and CMS XiO treatment planning systems, and gamma evaluation. The best HU improvement was observed in the developed In-House MAR. The maximum mean percentage differences in absorbed doses at the determined points in Accuray was found 33.3% and 32.5% between Without MAR - SMART MAR and Without MAR- In-House MAR, respectively. The In-House MAR software developed by using MATLAB was shown similar results with the SMART MAR software. Although in-house MAR software needs to be investigated clinically, it is more advantageous than commercially available software in terms of being cost-free, applicability in a shorter time and without reconstruction.

Introduction

In radiotherapy (RT), for the delineation of tumours and organs under risk, the computed tomography (CT) data are used in combination with other imaging methods [1]. The CT is also the basis for calculating the patient dose distributions [2]. During the CT imaging process, high-density materials such as implants for hip replacement, dental fillings, or surgical clips can cause metal artefacts [3]. A combination of mechanisms such as photon starvation, beam hardening, scattering and partial volume effects leads to metal artefacts [4]. Because of the polychromatic nature of x-ray beams, beam hardening occurs in CT systems. In addition, due to the hardening and scatter of the beam, dark streaks are formed [5]. As the CT radiation beam transmits through the patient or phantom, the lower energy component of the beam attenuates at a higher rate than the higher energy photons. As a result, the transmitted beam gets hardened and pitting or dark band artefact occurs between the dense materials in the images. Also, when a metal with a high atomic number attenuates the x-ray beam strongly, photon starvation artefacts occur because the number of photons reaching the detector decreases [3]. This situation causes difficulties in the identification of anatomical structures in CT images and leads to changes in the CT numbers, called Hounsfield Unit (HU) of the structures, due to missing data [6]. Inaccuracies in the HU values cause an error in the electron density or stopping power estimation, which significantly affects the dose calculation and optimization processes [7, 8]. This is a dosimetric problem that may cause errors in the evaluation of the dose distribution of the patient to be treated.

There are two main methods proposed in the literature for reducing metal artefacts. First of these is dual-energy computed tomography (DECT) virtual monochromatic (VM) extrapolations and it has been found that DECT VM images between 95 and 150 kilo electron Volt (keV) levels reduce artefacts of beam hardening from various metallic prostheses effectively [9, 10]. The second method is the use of the

iterative MAR algorithms [11, 12]. Various MAR algorithms have been developed to reduce metal artefacts [13].

Some of the MAR methods are interpolation-based sonogram correction, non-interpolation-based sonogram correction, hybrid sonogram correction, iterative image reconstruction, and image-based approaches [13]. Generally, in MAR methods, the projections passing through a metal section in patient data are replaced with interpolated data from neighbouring projections [14]. Because of the CT images disrupted by metal artefacts, there are many studies on the implications of metal artefacts in CT images for radiation therapy [15-17]. Performances of various MAR algorithms have been usually evaluated in terms of their ability to improve accurate anatomical structure definition and dose calculation for RT. While some studies have shown that commercial MAR algorithms play an important role in reducing the metal artefact effect and improving dose calculation accuracy, some other studies have revealed that the dosimetric effect between MAR-corrected and uncorrected images is not clinically significant [18-23].

In this study, we developed an alternative in-house software for CT MAR by using MATLAB (R2016a, USA) environment. The software in question was designed in a way that it could process images on another computer regardless of the CT device. The main purpose here was to seek an alternative method to eliminate this dosimetric problem without a commercial MAR algorithm.

Materials And Methods

Phantom Arrangement and CT Procedures

In this study, for the arrangement of phantoms (Fig. 1), two 5 mm bolus materials were placed on top of the 50 mm water equivalent solid phantom (SP34 white polystyrene IBA Dosimetry GmbH, Germany). Metals, which had dimensions of 31 x 31 x 2 mm (left) and 31 x 31 x 3 mm (right), were placed between two boluses and 20 mm beyond the phantom edge. Then, 50 mm solid phantoms were placed on the bolus (Fig.1). The schematic representation of the phantom arrangement from the top (a) and front (b) views are given in Fig. 1. Although, most metal hip prostheses are made of titanium with a much lower atomic number ($Z=22$), a lead plate with a high atomic number ($Z = 82$) was used in this study. The reason for this was to investigate the accuracy of the developed in-house software primarily for metals with high atomic number.

Axial images of this phantom were obtained at a slice thickness of 0.625 mm and 120 kVp tube voltage on CT (General Electric Healthcare, Chicago, IL, USA). These images obtained from CT were considered to be the original set with metal effect without MAR correction (Without-MAR). On these CT images, two corrected image sets were created through a commercial MAR algorithm (Smart-MAR) and through the in-house software (In-House MAR) developed in MATLAB environment. All dosimetric comparisons were evaluated for these three different sets of images. The extended CT-scale application was not used, and the metal HU value was fixed as 3071.

Performing corrections on the original CT images by using the developed in-house software

In this study, the in-house software was developed by using the MATLAB computer program to be able to correct CT images effectively. Before starting the image processing, CT images (without-MAR correction) of the phantom were transferred to the computer in DICOM format. For the conversion process, the first step is image segmentation. Image segmentation can be described as the division of images into regions corresponding to the structure of interest. To achieve the image segmentation process, maximum HU value (Metals HU value) is determined first in the entire image and this value is assigned as the threshold value. In this study also, CT images were segmented based on the determined threshold value (HU value of metal). Then, by using MATLAB Image Processing Toolbox, artefact image maps, which were called scattering patterns showing the scattering caused by high-density structures, were created. Except for the metal structure that creates artefact in the image, patterns of the high-density structures such as couch (other pattern) were removed from the scattering pattern and the image of the main pattern was obtained (Fig.2).

The second step of the conversion process is the application of the median filter. Median filter not only helps to reduce noise and smooth the signal but also preserves sharp details. The median filter, a nonlinear filter, is also available as standard in the MATLAB toolbox. However, when the median filter in the MATLAB toolbox is applied to the entire image, it causes all HU values in the image to change. Therefore, it is necessary to apply the median filter only to the area where the artefact is dense. So, median filter codes were rewritten to make field limitations on the scattering pattern and in this way the in-house MAR software was developed. Then, the rewritten median filter code was applied to original CT slices. Finally, CT images corrected by using the in-house MAR software developed in the MATLAB program were obtained in DICOM format. In the context of this study, CT images corrected by the developed in-house MAR software were called In-House MAR (IM).

Procedures in the Treatment Planning Systems (TPS)

Before the mentioned phantom arrangement, the HU values and standard deviations of the water equivalent solid water phantom and bolus materials used in the study were found. The mean HU values were obtained along circles with a 10 and 30 - pixel -diameter (mm) region of interest, whose center was defined in the same coordinate metal-free phantom (Fig. 3a), and which extended laterally from both metal edges in transverse slices for Without-MAR (WM), Smart-MAR (SM) and IM images (Fig. 3b).

CT images were transferred to the CMS XiO (CMS Co., St. Louis, MO, USA) and Accuray Precision (Accuray Co., USA) treatment planning systems (TPSs). The treatment plans were calculated on WM, SM and IM images by using 6 MV photon energy, superposition algorithm/step&shoot and superposition & convolution algorithm/helical, respectively in CMS XiO and Accuray Precision TPSs. While 5 different treatment plans were obtained in the CMS XiO TPS by using the Intensity Modulated Radiation Therapy (IMRT) technique for the linear accelerator device, 5 different treatment plans were created in the Accuray Precision TPS by using the helical IMRT technique for the Tomotherapy device. The percentage differences between absorbed dose values obtained from three image series (WM-SM, WM-IM, SM-IM)

were calculated for two planning systems. The locations of the selected absorbed dose points are shown in Fig. 1(a) and the distance between the determined points was 10 mm.

In addition, dose distributions on the WM, SM and IM transverse and coronal slices were calculated in CMS XiO, and compared with each other (WM-SM WM-IM and SM-IM). The difference in dose distributions in the transverse and coronal planes was evaluated using the gamma passing rate (GPR) in the OmniProl'mRT software. (IBA Dosimetry, Schwarzenbruck, Germany). In this study, the GPR ($\gamma < 1$) was performed according to $\Delta D = 1\%$ (dose difference parameter) and $\Delta d = 1$ mm (distance to agreement parameter) criteria.

Statistical analysis

Data analysis was performed using IBM SPSS Statistics version 20.0 (IBM, Istanbul, Turkey). The Kolmogorov–Smirnov test was used to check normality of variables. Statistical analysis for comparisons of groups was evaluated by using Kruskals-Wallis followed by the Mann Witney U. $p < 0.05$ was considered statistically significant.

Results

The results of this study obtained that metal sizes in the coronal axis of the original images (WM) appeared clearly larger than the actual size (Fig. 4). The right metal was measured approximately 51 mm, while the left metal was measured 48 mm. In both SM and IM images, it was seen (31mm) that the metals were in their real size (Fig. 4(b) and Fig. 4(c)).

In the transverse axis, images with the same window width (3000) and length (300) for WM, SM and IM are shown in Fig. 5 (a), (b), and (c), respectively. As seen in Fig. 5 (a), there are dark lines between right and left metals in the WM image. On the other hand, it is seen in Fig. 5 (c) that both the dark lines towards the lateral and the brightness around the metal are considerably reduced in the IM image.

The mean HU values and standard deviations of the metal-free water-equivalent and metal-containing phantom arrangements are shown in Table 1. It was shown that the mean HU value increases while the radius of the circle area on the edge of the metals decreases. It was found that the mean difference between WM_{left} and IM_{left} was 179HU (-247 and -68), and the difference between WM_{Right} and IM_{Right} was 273HU (-369 and -96) for 30mm. The biggest difference between IM and metal-free water-equivalent images was found as 160 HU (4 and -156) in a circle with a diameter of 10 mm on the right side of the metal. On the other hand, the biggest difference between SM and metal-free water-equivalent images was found as 441 HU (4 and -445) in a circle with a diameter of 10 mm.

Table 1. The HU values and standard deviations of the circle regions.

		Circle Radius			
		30 mm		10 mm	
		HU	SD	HU	SD
Without Metal	Solid Phantom	5	±3	4	±7
	Bolus Material	-6	±4	-1	±9
With Metal	Without-MARright	-369	±362	-918	±244
	Smart-MARright	-131	±166	-445	±289
	InHouse-MARright	-96	±85	-156	±220
	Without-MARleft	-247	±391	-760	±409
	Smart-MARleft	-104	±189	-422	±295
	InHouse-MARleft	-68	±103	-123	±207

The absorbed dose values (cGy) were calculated at the determined points (for right side; -4,-5,-6,-7,-8,-9,-10 and for left side; 4, 5, 6, 7, 8, 9, 10) in the WM, SM and IM images for both TPSs. Then, the percent differences of absorbed dose (PDAD) values between WM-SM, WM-IM, and SM-IM at the points determined in Fig. 1a were calculated. In both TPSs, the mean PDAD values of 5 treatment plans were obtained. The graphs where the determined points correspond to the mean PDADs are shown in Fig. 6 and Fig. 7 for the CMS XiO and Accuray TPSs, respectively.

As seen Fig. 6, the maximum mean PDAD value at the determined points in CMS XiO was found at point “-7” on the left side (6.05%) between WM and SM, while it was obtained at point “8” (8.05%) on the right side. While the maximum difference between WM and IM was found at point “-8” (6.18%) on the right side, it was obtained at point “8” (8.77%) on the right side. The PDAD values between SM and IM were less than 2% at all points except for the value of 2.58% found at point “9”. In SM and IM plans, mean percentage differences were found as 0.66 % (0.04% -2.58%) for the CMS XiO TPS. The difference between WM-SM and WM-IM was found statistically significant ($p \leq 0.05$) except for -10, -8 and 6 points ($p > 0.05$). The differences at all points were statistically significant ($p \leq 0.05$), both between WM-SM and SM-IM, and between WM-IM and SM-IM.

The maximum mean PDAD value at the determined points in Accuray Precision was found at point “-7” on the right side (33.3%) between WM and SM, while it was obtained at point “8” (33.3%) on the left side. The maximum difference between WM and IM was found at point “-8” (30.1%) on the right side, it was obtained at point “7” (32.5%) on the left side. The PDAD values between SM and IM were less than 3.5% at all points except for the values of 5.9% and 6.8% found at points “-9” and “9”, respectively (Fig. 7). The difference between WM-SM and WM-IM was found statistically significant ($p \leq 0.05$) except for “-4” and “8” ($p > 0.05$). The differences at all points were statistically significant ($p \leq 0.05$), both between WM-SM and SM-IM, and between WM-IM and SM-IM.

Table 2 shows the gamma passing rates between the WM-SM, WM-IM and SM-IM dose maps of each plan obtained on coronal and transverse slices in the CMS XiO TPS. For transverse slices, minimum and maximum gamma passing rates between WM and IM images were found to be 62.52% -74.5%, respectively, while the minimum gamma passing rate between SM and IM images was found to be 95.81%. It was found that the improvement was 8.33% and 8.64% for SM and IM, respectively in the coronal plane ($p < 0.05$), while it was 26.03% and 25.24% in the transverse plane ($p < 0.05$). In both planes, GPR differences between MAR applied and unapplied images are statistically significant, although the larger increase in the transverse plane indicates that the depth-dependent dose variation of the metal-containing region is more remarkable.

Table 2 The gamma passing rates and mean values between the WM-SM, WM-IM and SM-IM dose maps of each plan obtained on coronal and transverse slices on CMS XiO TPS

		Gamma passing rates (%)					
		Plan I	Plan II	Plan III	Plan IV	Plan V	Mean
Coronal Slices	WM-SM	88,35	89,24	88,57	88,62	91,19	89,19
	WM-IM	89,23	89,69	88,60	88,63	91,36	89,50
	SM-IM	96,94	98,63	97,97	97,95	97,66	97,83
Transverse Slices	WM-SM	68,41	62,51	73,68	71,45	74,45	70,10
	WM-IM	67,47	66,45	72,71	73,27	74,56	70,89
	SM-IM	96,14	96,27	95,81	96,08	96,34	96,13

In Fig. 8, for WM-SM (a), WM-IM (b) and SM-IM (c) treatment plans, the dose distributions, profile curves in which the two plans are compared, and gamma passing maps are presented on the coronal plane. In addition, dose distributions, profile curves, and gamma passing maps in the transverse plane are also presented for WM-SM, WM-IM, and SM-IM in Fig. 8 (d), (e), and (f), respectively. In the gamma passing maps given in Fig. 8, the red regions indicate that the dose differences are higher than the acceptance value ($\gamma \geq 1$).

Discussion

Artifacts in the form of streaks caused by metal implants give rise to photon starvation in CT and dosimetric problems in radiotherapy planning. In CT images, the loss of anatomical information and the use of wrong HU causes errors in RT dose calculations, and this also leads to inadequate patient treatment [24].

This study focused on producing metal artefact-corrected CT images that could be directly used for creating RT plans. For this purpose, an in-house MAR (IM) software was developed using the MATLAB

environment. An advantage of this developed software is that it does not require access to proprietary data of the scanning equipment such as sinogram data or the computation of a virtual sinogram. Since the developed method is only based on operations such as median and mean calculations of CTs obtained from the usual and validated workflow, the reliability of the method can be easily determined. The safety of this method can be easily established and the post-processing step is quite transparent when the validity of the calculated CT number is concerned. Moreover, the accuracy of CT number is improved when the MAR algorithm is applied.

In this study, although the commercial MAR algorithm provided a highly improved dataset, some residual artefacts were still observed in the corrected images. Similar observation was also reported by other studies [5, 25]. On the other hand, it was found that the IM tended to reduce the residues in the improved images a little more (Fig. 2).

In the WM images, HU is significantly affected by metal artefacts. Jarriault, & Lanaspèze found that HU errors were close to 20% for titanium hip replacement and 50% for steel hip replacement [26]. In the same study, the correction was performed with the commercial MAR software, and the mean HU values of metal-containing CT images and non-metal-containing CT images were compared; finally, it was concluded that the results varied by 2%. It was determined that the biggest difference between WM and IM mean HU values were 762 (-918 and -156) and 273 (-369 and -96) within the 10mm and 30mm circles, respectively [26]. Katsura et al. reported that projection-based commercial MAR algorithms had quite positive effects on the correction of HU values [27]. Our study also shows that photon starvation becomes more pronounced in metals with higher atomic numbers, but still, both the SM and IM algorithm have the same positive effect on CT images containing metal.

Ohira et al and De Crop et al reported that for metallic material with higher density, both the objective and subjective image qualities were found to decrease more [28, 29]. Also, they reported that as the number of metal implants increased, the severity of metal artefacts increased. Spede et al noticed that the impact of MAR on dosimetry was dependent on the atomic number of the metal [30]. They reported that low Z materials, such as titanium ($Z = 22$), did not produce significant dose errors whereas high Z materials, such as platinum ($Z = 78$), could substantially affect the dose calculation. They also found that the maximum dose difference of high Z material was 20%-25% in the region surrounding the metal [30]. In this study, the maximum absorbed dose percentage difference was observed in the vicinity of the metal artefact region in both Accuray and CMS XiO treatment planning systems. For both planning systems, the dose differences between WM and IM at points close to the hip prosthesis (mines and plus "7", "8", "9", and "10") were more distinct than the difference between WM and SM. Nevertheless, mean percentage dose differences were in Accuray greater than XiO. The dose differences between IM and SM were quite small. The small difference is an indication that the in-house software is as successful as the commercial software for metal artefact reduction.

To be able to assess dose calculation accuracy, the dose distributions for transverse and coronal slices were evaluated using a gamma analysis in this study. Both coronal and transverse slices, out-of-limit

regions are seen in red. As a result of the gamma evaluation, it was observed that the dose distribution using both SM and IM was significantly improved compared to that of the uncorrected images (WM).

The limitation of this study is that IM software is not tested on real patient CT images containing prostheses. The next step of this study is to investigate this limitation.

Conclusion

In this study, to be able to reduce metal artefact, an in-house MAR software was developed in MATLAB environment. The effectiveness of this developed software was examined by comparing the CT images corrected by the in-house MAR software with both the CT images corrected by the commercial Smart MAR software and the CT images without MAR correction. Results revealed the success of the developed method. The advantages of the in-house developed method under conditions of sufficient complementary information include the successful reduction of metal artefacts in the reconstructed images. Unlike the MAR methods that are commonly used and require sinogram data, the developed method consists of the post-processing procedure that can be performed without the need for a CT system or reconstruction method. Although the MAR-corrected CT scan requires extra time and cost, the developed IM can reduce the time CT will be occupied and it is cost-free. In addition, to be able to perform MAR correction on CT in the pelvic radiotherapy of patients with hip-prosthetics, this software is upgradeable.

Declarations

Funding

The study was not supported by any institution or organization.

Conflict of interest

The authors declare that they have no conflict of interest.

Author Contributions

All authors contributed equally.

Ethical Statement

This article does not contain any studies with human participants or animals performed by any of the authors.

References

- [1] Maerz M, Koelbl O, Dobler B (2015.) Influence of metallic dental implants and metal artefacts on dose calculation accuracy. *Strahlentherapie und Onkologie*, 191: 234–41.
- [2] Chu JC, Ni B, Kriz R, Amod Saxena V (2000). Applications of simulator computed tomography number for photon dose calculations during radiotherapy treatment planning. *Radiotherapy and Oncology*, 55: 65–73.
- [3] Huang V, Kohli K (2017). Evaluation of New Commercially Available Metal Artifact Reduction (MAR) Algorithm on Both Image Quality and Relative Dosimetry for Patients with Hip Prosthesis or Dental Fillings. *International Journal of Medical Physics, Clinical Engineering and Radiation Oncology*, 5(7): 124-38.
- [4] De Man B, Nuyts J, Dupont et al (1999). Metal streak artifacts in x-ray computed tomography: a simulation study. *IEEE Transactions on Nuclear Science*, 46 (3): 691–696.
- [5] Boas FE, Fleischmann D (2011). Evaluation of Two Iterative Techniques for Reducing Metal Artifacts in Computed Tomography. *Radiology*, 259: 894-902.
- [6] Bar E, Schwahofer A, Kuchenbecker S, Haring P (2015). Improving radiotherapy planning in patients with metallic implants using the iterative metal artifact reduction (iMAR) algorithm. *Biomedical Physics Engineering Express*, 1, 025206.
- [7] Bedford JL, Childs PJ, Nordmark Hansen V et al (2003). Commissioning and quality assurance of the Pinnacle3 radiotherapy treatment planning system for external beam photons. *The British Journal of Radiology*, 76: 163–76.
- [8] Kim Y, Tome WA., Bal M et al (2006). The impact of dental metal artefacts on head and neck IMRT dose distributions. *Radiotherapy and Oncology*, 79: 198–202.
- [9] Bamberg F, Dierks A, Nikolaou K, Reiser MF et al (2011). Metal artifact reduction by dual energy computed tomography using monoenergetic extrapolation. *European Radiology*, 21: 1424–9.
- [10] Wang Y, Qian B, Li B et al (2013). Metal artifacts reduction using monochromatic images from spectral CT: Evaluation of pedicle screws in patients with scoliosis. *European Journal of Radiology*, 82, 360 – 6.
- [11] Lell MM, Meyer E, Schmid M et al (2013). Frequency split metal artefact reduction in pelvic computed tomography. *European Journal of Radiology*, 23: 2137–45.
- [12] Meyer E, Raupach R, Lell M et al (2010). Normalized metal artifact reduction (NMAR) in computed tomography. *Medical Physics*, 37 (10), 5482-93.
- [13] Abdoli M, Dierckx RA, Zaidi H (2012). Metal artifact reduction strategies for improved attenuation correction in hybrid PET/CT imaging. *Medical Physics*, 39: 3343–3360.

- [14] Gjestebj L, De Man B, Jin Y et al (2016) Metal artifact reduction in CT: where are we after four decades? *IEEE Access*, 4: 5826–49.
- [15] Giantsoudi D, De Man B, Verburg J et al (2017). Metal artifacts in computed tomography for radiation therapy planning: dosimetric effects and impact of metal artifact reduction. *Physics in Medicine & Biology*, 62 (8): 49–80.
- [16] Mail N, Albarakati Y, Khan MA et al (2013). The impacts of dental filling materials on RapidArc treatment planning and dose delivery: challenges and solution. *Medical Physics*, 40 (8), 081714.
- [17] Son SH, Kang YN, Ryu MR (2012). The effect of metallic implants on radiation therapy in spinal tumor patients with metallic spinal implants. *Medical Dosimetry*, 37, 98–107.
- [18] Morsbach F, Bickelhaupt S, Wanner GA et al (2013). Reduction of metal artifacts from hip prostheses on CT images of the pelvis: value of iterative reconstructions. *Radiology*, 268, 237– 44.
- [19] Morsbach F, Wurnig M, Kunz DM et al (2013). Metal artefact reduction from dental hardware in carotid CT angiography using iterative reconstructions. *European Radiology*, 23, 2687– 94.
- [20] Maerz M, Mittermair P, Krauss A et al (2016). Iterative metal artifact reduction improves dose calculation accuracy. *Strahlentherapie und Onkologie*, 192: 403– 13.
- [21] Axente M, Paidi A, Von Eyben R et al (2015). Clinical Evaluation of the Iterative Metal Artifact Reduction Algorithm for CT Simulation in Radiotherapy. *Medical Physics*, 42: 1170-1183.
- [22] Li H, Noel C, Chen H et al (2012). Clinical Evaluation of a Commercial Orthopedic Metal Artifact Reduction Tool for CT Simulations in Radiation Therapy. *Medical Physics*, 39: 7507-17.
- [23] Shen ZL, Xia P, Klahr P, Djemil T (2015) Dosimetric Impact of Orthopedic Metal Artifact Reduction (O-MAR) on Spine SBRT Patients. *Journal of Applied Clinical Medical Physics*, 16, 106-116.
- [24] Guilfoile C, Rampant P, House M (2017). The impact of smart metal artefact reduction algorithm for use in radiotherapy treatment planning. *Australasian Physical & Engineering Sciences in Medicine*, 40: 385– 94.
- [25] Jeong S, Kim SH, Hwang EJ et al (2015). Usefulness of a Metal Artifact Reduction Algorithm for Orthopedic Implants in Abdominal CT: Phantom and Clinical Study Results. *American Journal of Roentgenology*, 204: 307-317.
- [26] Jarriault AA, Lanaspese C (2018). 19 Assessment of Smart MAR (Metal Artifact Reduction) algorithm for metallic artifact correction in external radiotherapy planning. *Physica Medica: European Journal of Medical Physics*, 56(1):49.

[27] Katsura M, Sato J, Akahane M et al (2018). Current and Novel Techniques for Metal Artifact Reduction at CT: Practical Guide for Radiologists. Radiographics, 38 (2): 450-461.

[28] Ohira S, Kanayama N, Wada K et al (2018). How Well Does Dual-Energy Computed Tomography With Metal Artifact Reduction Software Improve Image Quality and Quantify Computed Tomography Number and Iodine Concentration? Journal of Computer Assisted Tomography, 42(4), 655-660.

[29] De Crop A, Casselman J, Van Hoof T et al (2015). Analysis of metal artefact reduction tools for dental hardware in CT scans of the oral cavity: kVp, iterative reconstruction, dual-energy CT, metal artifact reduction software: does it make a difference? Neuroradiology, 57: 841–849.

[30] Spadea MF, Verburg JM, Baroni G, Seco J (2014). The impact of low - Z and high - Z metal implants in IMRT: a Monte Carlo study of dose inaccuracies in commercial dose algorithms. Medical Physics, 41, 011702.

Figures

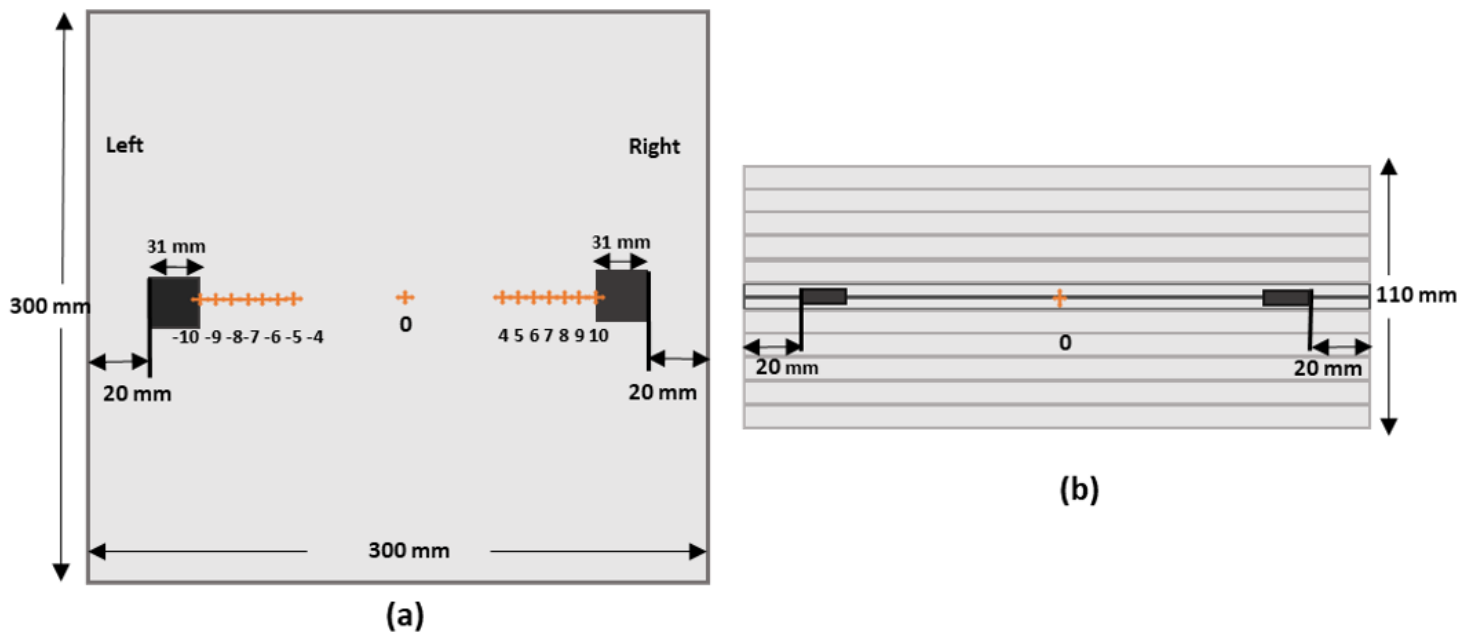


Figure 1

Schematic representation of the top view of the phantom arrangement and the points given at 10 mm intervals from the right/left edge of the metals (a). Schematic representation of the front view of the phantom arrangement (b)

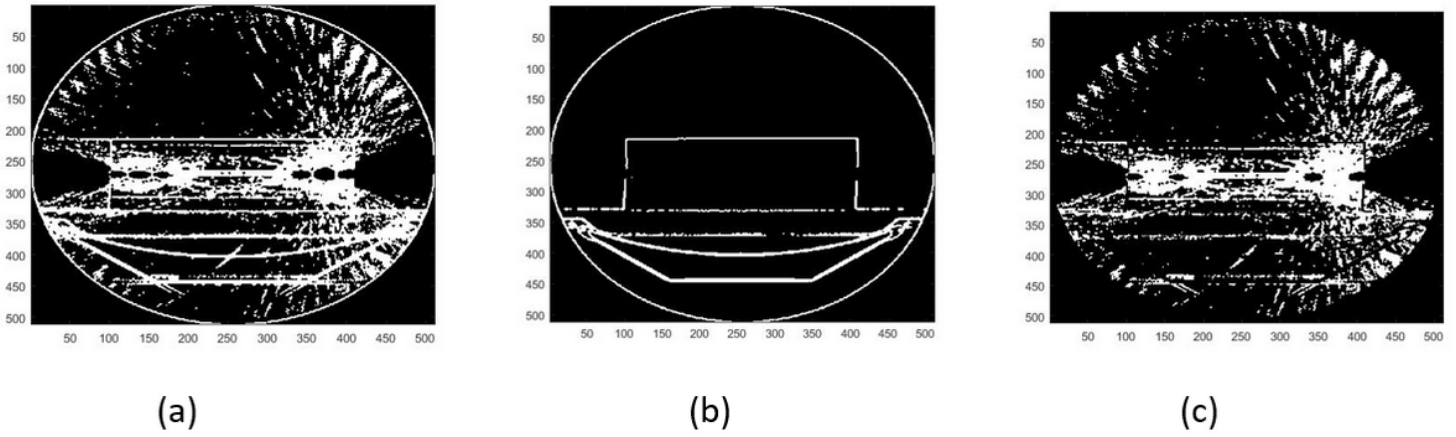


Figure 2

Scattering pattern showing scattering caused by high-density structures (a). The other pattern showing high-density structures other than metal (b). The main pattern obtained by removing the other pattern from the scattering pattern (c).

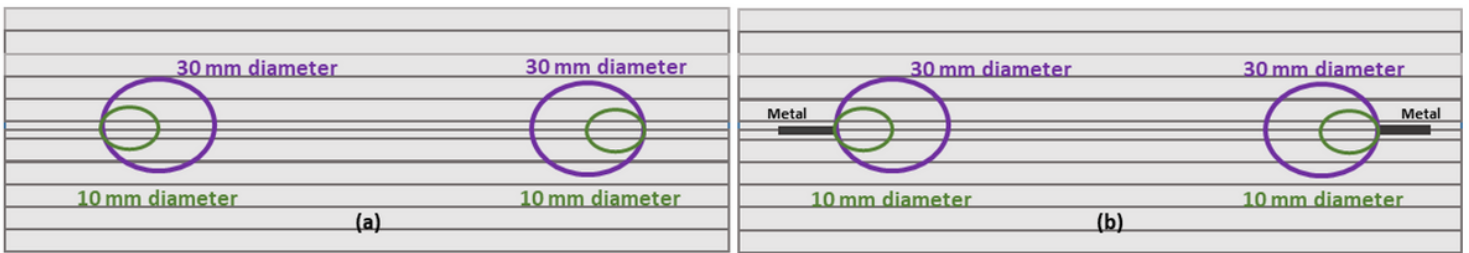


Figure 3

3 Circles with diameter of 10 and 30 mm, whose center was defined in the same coordinate metal-free phantom (a), and which extended laterally from both metal edges in transvers slices for WM, SM and IM images (b).

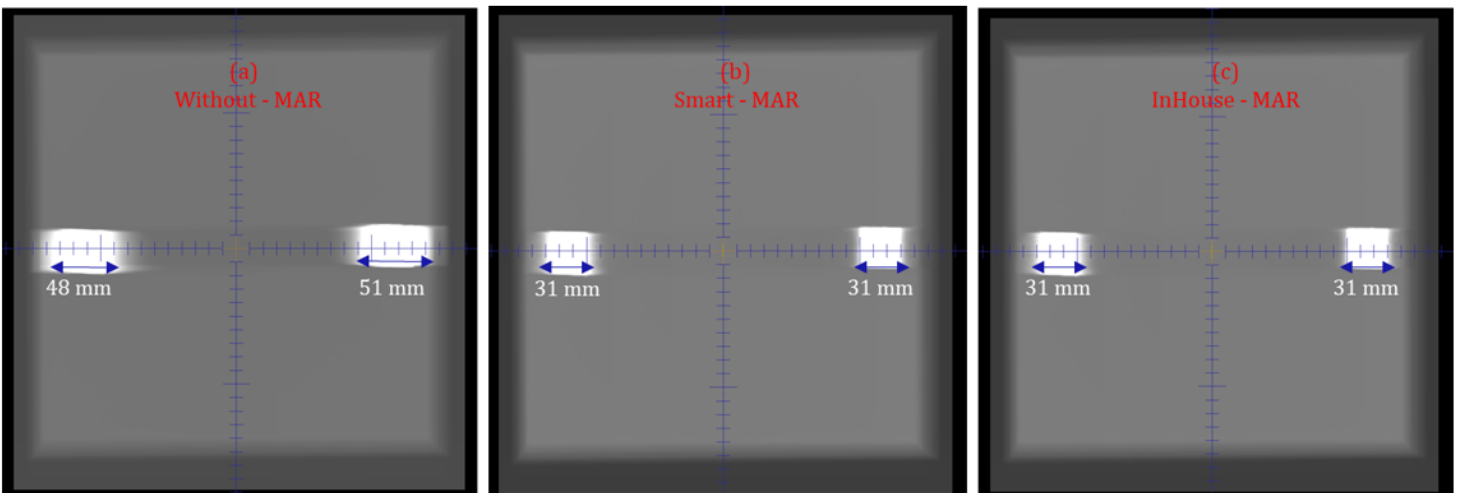


Figure 4

The Digitally Reconstructed Radiographs (DRR) images for WM (a), SM (b) and IM (c).

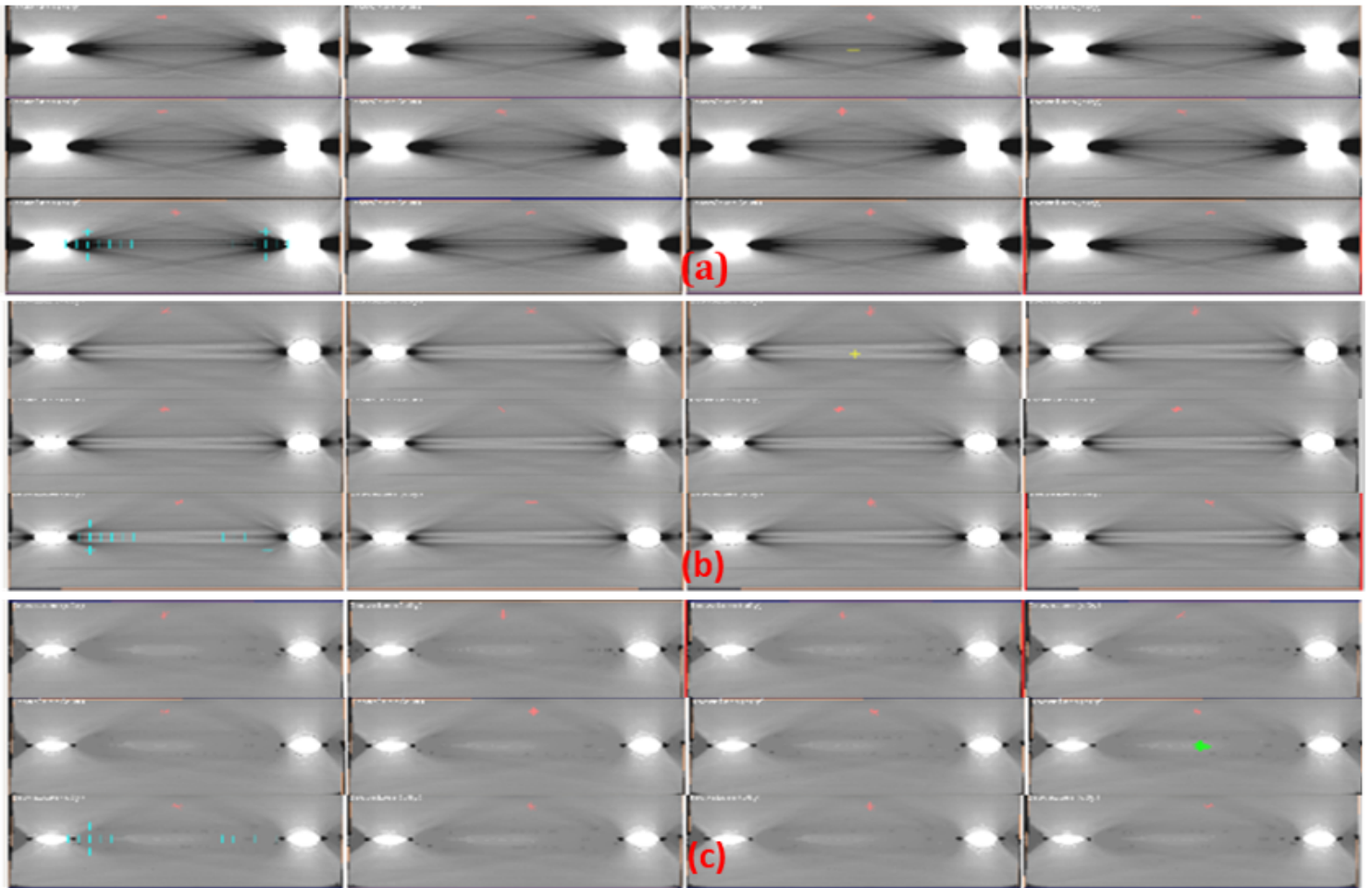
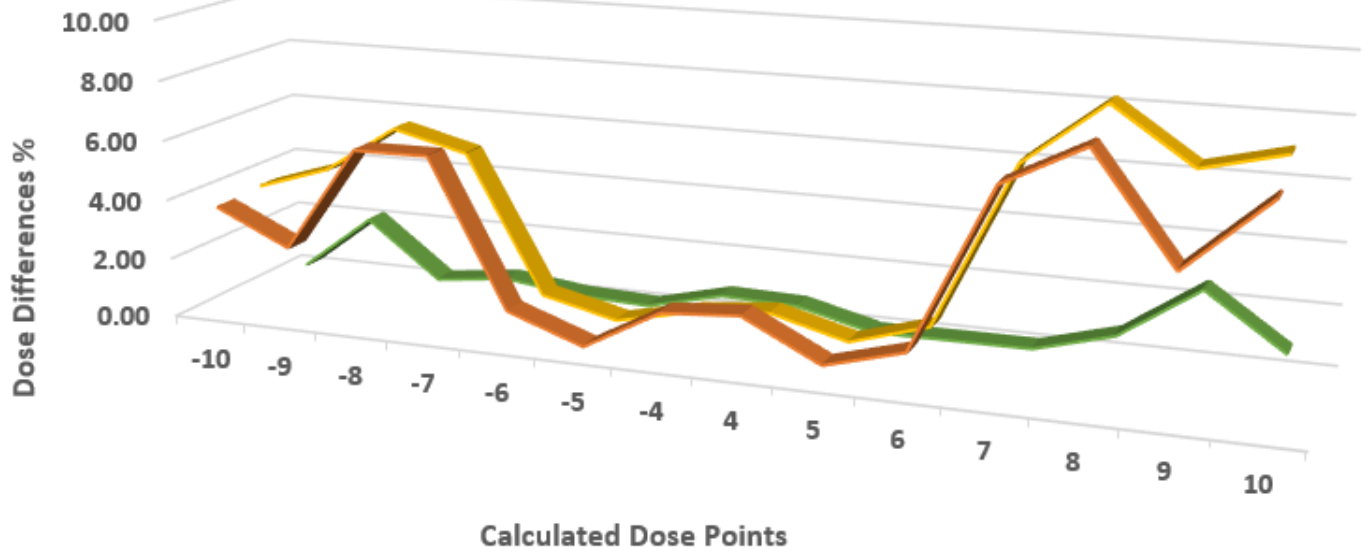


Figure 5

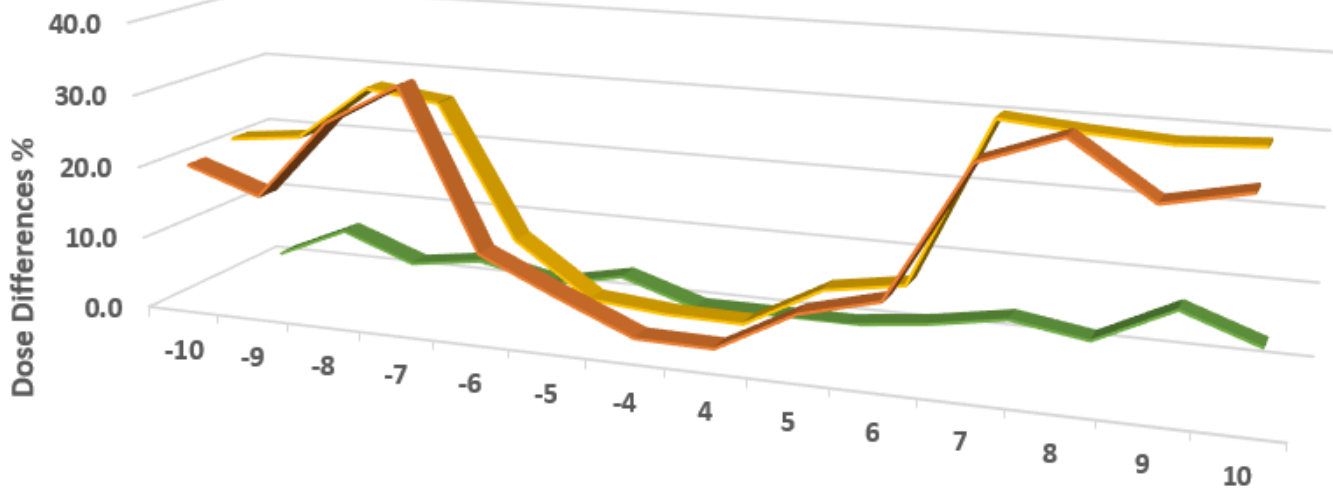
In the transverse axis, images with the same window width (3000) and length (300) for WM (a), SM (b), and IM (c)



	-10	-9	-8	-7	-6	-5	-4	4	5	6	7	8	9	10
WM-SM	3.68	2.53	6.03	6.05	1.20	0.30	1.70	1.89	0.59	1.31	6.71	8.05	4.62	6.98
WM-IM	3.77	4.57	6.18	5.55	0.98	0.38	0.95	1.20	0.53	1.32	6.74	8.77	7.01	7.65
SM-IM	0.26	2.16	0.24	0.54	0.22	0.12	0.74	0.67	0.04	0.07	0.08	0.80	2.58	0.78

Figure 6

The mean Percent Dose Differences of 5 treatment plans on CMS XiO TPS



	Calculated Dose Points													
	-10	-9	-8	-7	-6	-5	-4	4	5	6	7	8	9	10
WM-SM	20.0	16.5	27.6	33.3	11.5	6.8	2.3	2.2	8.0	10.8	29.3	33.3	26.2	28.5
WM-IM	21.3	22.4	30.1	28.8	10.6	3.3	2.3	2.2	8.0	9.8	32.5	31.5	30.9	31.5
SM-IM	1.4	5.9	2.0	3.5	1.2	3.4	0.0	0.0	0.0	1.2	3.1	1.4	6.8	2.9

Figure 7

The mean Percent Dose Differences of 5 treatment plans on Accuray Precision TPS

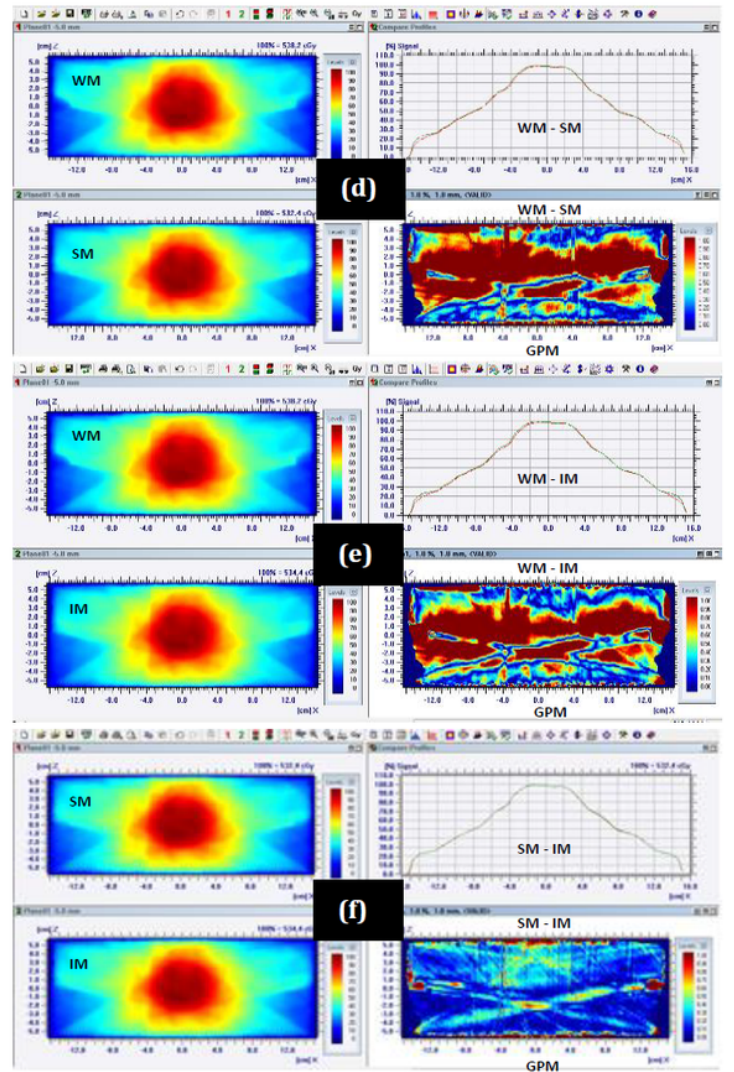
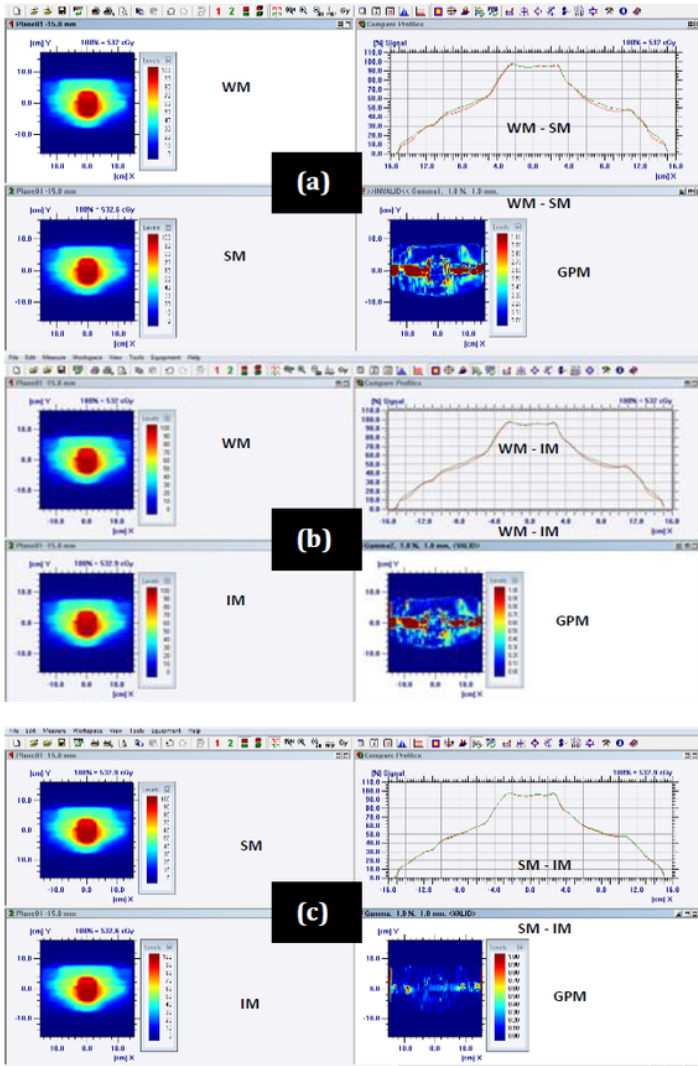


Figure 8

For WM-SM (a), WM-IM (b) and SM-IM (c) treatment plans, the dose distributions, profile curves in which the two plans are compared, and gamma passing maps (GPM) images on the coronal plane. For WM-SM (d), WM-IM (e) and SM-IM (f) treatment plans, the dose distributions, profile curves in which the two plans are compared, and gamma passing maps (GPM) images on the transverse axis. The points where the gamma evaluation failed shown in red.